Channel Propagation Characteristics for Massive Multiple-Input/Multiple-Output Systems in a Tunnel Environment

Asad Saleem, Haixia Cui, Yejun He, and Amir Boag

The effect of delay spread (DS), the specular multipath components (SMCs), and the impact of dense multipath components (DMCs) on multiple-input/multiple-output (MIMO) system performance in a tunnel environment are studied by considering a Richter's maximum-likelihood (RiMAX)-based estimator. The path loss (PL), angular spread, interuser spatial correlation, and capacity of a massive MIMO framework are analyzed at the 3.5-GHz frequency band through a measurement campaign inside a subway tunnel to implement the latest 5G standards. The radio channel consists of a uniform rectangular array of 32 transmitting elements and a uniform cylindrical array of 64 receiving elements with horizontal and vertical polarizations. The power ratio of the DMCs is found to be distance dependent, as the DMCs and SMCs behave differently in tunnels. Moreover, the study shows that the channel capacity, angular spread, and DS are reduced as the distance between the transmitting and receiving antenna arrays increases, whereas the PL exponent increases with the distance. This research highlights the importance of considering spatial

EDITOR'S NOTE

In this issue's "Measurements Corner" column, the authors conduct a campaign at the 3.5-GHz frequency band for a 32 × 64 massive multiple-input/multiple-output (MIMO) radio channel in a tunnel. The channel power delay profile, root-mean-square delay spread, path loss, angular spread, interuser spatial correlation, and capacity are analyzed for four polarization schemes to implement next-generation radio propagation standards. A Richter's maximum likelihood-based algorithm is used to compute the specular components and dense multipath components. This research provides guidance to enhance the accuracy of 5G massive MIMO system models in underground mobile communications.

Xiu Yin Zhang

characteristics in 5G massive MIMO system models and provides guidelines to enhance the networks' accuracy in underground mobile communications.

INTRODUCTION

Due to the growing use of tablets, mobile phones, laptops, and numerous other application services, user traffic on mobile networks is increasing remarkably. In recent years, next-generation radio communication networks, such as 5G [1], have been broadly explored to facilitate the growing demand for data traffic. Massive MIMO is considered an emerging cutting-edge technology capable of fulfilling the advanced requirements of the 5G [2] to handle ever-growing demand for various vehicle-to-vehicle communications [3].

Increasing the number of base station antennas can mitigate the influence of small-scale fading (SSF) and minimize interuser correlation by adopting spatial division to simultaneously configure discrete beams [4]. The linear precoding technique can be adopted [5] and becomes almost optimal when the number of transmitting and receiving antennas increases [6]. Accurate modeling of a massive MIMO channel, including its interuser correlation and fundamental propagation characteristics, is essential for designing wireless systems.

SMCs (consisting of reflected waves) are well described in channel propagation models but not strictly the only contributors. DMCs (including weak SMCs and diffuse scattering) were initially reported in [7] and are now universally

acknowledged as important radio channel components for indoor environments [8]. DMCs can be extracted from the channel impulse response (CIR) as declining exponential residual power delay profiles (PDPs) after SMCs are removed. In general, it is recognized that the impact of DMCs on the overall received power is significant at higher frequency bands for confined environments and that it reduces as the frequency of a channel increases [7]. Polarimetric massive MIMO channel measurements at 1.3 GHz in a factory setting were investigated, revealing that diffuse components' power contribution changes between 10% and 95% depending on the transmitting–receiving distance and line-of-sight (LOS) propagation paths [9]. In [10], the behavior of distance-based DMC parameters was investigated in a subway tunnel at 11 GHz. Moreover, DMC parameters have been validated by considering an empirical cluster-based massive MIMO channel model.

Hence, several studies conclude that improved ray-tracing tools and DMC models are needed to enhance the accuracy of radio channel models, even at millimeter-wave (mm-wave) frequency bands [11]. Although some literature can be found on massive MIMO indoor channels, no one has revealed the relationship between SMCs and DMCs. Despite their prominent contributions in indoor radio channel models, one can say that the impact of diffuse components on various characteristics of massive MIMO networks, particularly correlation at the receiving end, has not been explored. Only in [12] was the spatial correlation at the receiving side associated with the phase variations of an antenna array in a confined environment at 1.8 GHz. Moreover, 5G bands, such as the 3.5-GHz one, need to be configured according to the Global System for Mobile Communications Association World Radiocommunication Conference series standards. To this end, further radio channel measurement campaigns in this frequency band are needed.

To study a MIMO system, spatial characteristics turn out to be as crucial as temporal characteristics. Many aspects of the MIMO channel, such as the singular distribution, PL, and capacity, are predicted by angular spread in [13]–[15]. The power angular spectrum (PAS) estimates the spatial characteristics of the receiver (Rx) in the azimuthal direction. Moreover, the angular spread was evaluated as the standard deviation of the PAS, which was proportional to the root-mean-square (RMS) DS of the PDP. In addition, it was shown that a greater angular spread results in a smaller correlation coefficient [13]. In [16], massive MIMO radio channel measurements were calibrated in an intrawagon scenario at mm-wave bands, and it was shown that the channel capacity is proportional to the frequency of a radio channel.

To the authors' best knowledge, existing MIMO systems do not consider high numbers of transceiver antennas, and studies based on long-distance vehicular communications in real subway tunnels are notably limited. In this article, we identify technical challenges and provide recommendations for future research, particularly in the area of smart rail transportation. The main contributions of this research can be summarized as follows:

1) We modify the traditional RiMAX algorithm for the joint estimation of DMCs' propagation parameters in the angular, polarization, and frequency domains to quantitatively analyze DMCs' characteristics across longer distances in a real-time environment. The distributions of path parameters, such as delays and angles, the polarization matrix, and the polarization ratio of DMCs, are investigated for a massive MIMO channel at 3.5 GHz.

2) This study is associated with diffuse components' power characteristics and their effect on the distance between transmitting and receiving antenna arrays. To the best of the authors' knowledge, this work considers, for the first time, a real-time massive MIMO channel measurement campaign.

3) The PL model, angular spread, RMS DS, and influence of the separating distance on the correlation and channel capacity are estimated, which is important for 5G indoor radio channel models.

GENERAL SYSTEM MODEL

We consider the baseband characteristics of a bidirectional channel [5], [6] to explain the contribution of the propagation path, SMCs, and a multivariate complex normal (Gaussian) distributed approach to investigate the DMCs of a radio channel [7].

PROPAGATION PATH AND DMC CHANNEL MODELING

According to ray optical modeling, the complex wave propagation in an environment containing a multitude of scattering, reflecting, and diffracting objects can be approximated by the superposition of multiple discrete waves. It is worth noting that the angles at the transmitter (Tx) and Rx are often determined in local coordinate systems. Figure 1 illustrates the basic propagation phenomena in a confined environment in the presence of multiple reflections, diffractions, and scattering events due to various objects. The characteristics of DMCs are well defined in [7]. This work considers the zero-mean complex Gaussian approach with a covariance matrix $R(\theta_{\text{dmc}})$ to describe the DMCs' contribution (d_{dmc}) to radio channel characteristics; i.e.,

$$d_{\text{dmc}} \sim N_c(0, R(\theta_{\text{dmc}})) \in C^{M \times 1}, \quad (1)$$

where M is the number of measurement data samples in a channel observation. The majority of measurement campaigns stipulate that DMCs be spatially uncorrelated, so their correlations are assumed to take place only in the frequency domain. Moreover, the covariance matrix has a Toeplitz structure in the frequency domain and is given by

$$R_f(\theta_{\text{dmc}}) = \text{toep}(m(\theta_{\text{dmc}}), m(\theta_{\text{dmc}})^H), \quad (2)$$

where $toep(.)$ is the Toeplitz operator, $(.)^H$ is the Hermitian transpose or the transpose conjugate of a matrix, and $m(\theta_{\text{dmc}})$ is the correlation function, which can be derived as

$$m(\theta_{\text{dmc}}) = \frac{\alpha_{\text{dmc}}}{M_f}\left(\frac{1}{\beta_{\text{dmc}}} \ldots\ldots \frac{e^{-j2\pi(M_f-1)\tau_{\text{dmc}}}}{\beta_{\text{dmc}} + j2\pi\frac{(M_f-1)}{M_f}}\right),$$
$$(3)$$

where the parameters β_{dmc}, α_{dmc}, τ_{dmc}, and M_f are the normalized coherence bandwidth, minimal attenuation, time delay of diffuse components, and number of frequency samples, respectively. Hence, DMCs' covariance matrix has the following configuration:

$$R(\theta_{\text{dmc}}) = I \otimes R_f(\theta_{\text{dmc}}), \qquad (4)$$

where $I \in C^{M \times M}$ is an identity matrix of size $M \times M$. Since each channel sounding includes measurement noise, we introduce an independent identically distributed Gaussian function to tackle the measurement noise $w_o \sim N_c$ $(0, I) \in C^{M \times 1}$. In total, one channel observation can be modeled as

$$x = \sqrt{\alpha_0} \cdot w_o + s(\theta_{\text{sp}}) + d_{\text{dmc}}, \qquad (5)$$

where α_o is the measurement noise variance.

Because DMCs and measurement noise are Gaussian circular processes, it seems logical from the perspective of parameter estimation to combine them in one step. Therefore, the initial channel observation is given by

$$x \sim N_c(s(\theta_{\text{sp}}), \alpha_o + R(\theta_{\text{dmc}}))$$
$$\sim N_c(s(\theta_{\text{sp}}), R(\theta_{\text{dan}})) \in C^{M \times 1}, \quad (6)$$

where $\theta_{\text{dan}} = [\mu_R, \mu_T, \kappa_R, \kappa_T, \gamma_{d,HH}, \gamma_{d,HV}, \gamma_{d,VH}, \gamma_{d,VV}]$, $\theta_{\text{dmc}} = [\alpha_o, \alpha_{\text{dmc}}, \beta_{\text{dmc}}, \tau_{\text{dmc}}]$,

and $\theta_{\text{sp}} = [\tau_{\text{sp}}, \phi_T, \theta_T, \phi_R, \theta_R, \gamma_i]$. Also, $\mu_R, \mu_T, \kappa_R, \kappa_T, \gamma_{d,HH}, \gamma_{d,HV}, \gamma_{d,VV}$, and $\gamma_{d,VV}$ represent the normalized azimuth of the angle of arrival (AoA), normalized azimuth of the angle of departure (AoD), angular spread of the von Mises distribution at the Rx side, angular spread of the von Mises distribution at the Tx side, path weight of the *HH* polarization, path weight of the *HV* polarization, path weight of the *VH* polarization, and path weight of the *VV* polarization for the DMCs, respectively. Moreover, $\tau_{\text{sp}}, \phi_T, \theta_T, \phi_R, \theta_R$, and γ_i represent the propagation delays, azimuth AoD, elevation AoD (EoD), azimuth AoA, and elevation AoA (EoA) for SMCs, and $\gamma_i = [\gamma_{s,HH}, \gamma_{s,HV}, \gamma_{s,VH}, \gamma_{s,VV}]$, respectively.

MAXIMUM-LIKELIHOOD APPROACH

Based on the parameters of given model θ_{sp} and θ_{dan}, the probability density function of an observation x is given by

$$p(x \mid \theta_{\text{sp}}, \theta_{\text{dan}}) = \frac{1}{\pi^M \det(R(\theta_{\text{dan}}))}$$
$$\times e^{-(x-s(\theta_{\text{sp}}))^H R^{-1}(\theta_{\text{dan}}) \cdot (x-s(\theta_{\text{sp}}))}. \quad (7)$$

In terms of the log-likelihood function, excluding constant terms, we have the following relationship:

$$\mathcal{L}(x \mid \theta_{\text{sp}}, \theta_{\text{dan}}) = -\ln(\mid R(\theta_{\text{dan}})\mid)$$
$$-(x-s(\theta_{\text{sp}}))^H R^{-1}(\theta_{\text{dan}}) \cdot (x-s(\theta_{\text{sp}})). \quad (8)$$

Since the vectors θ_{dan} and θ_{sp} are independent functional sets, we consider the space-alternating generalized expectation–maximization (SAGE) algorithm [17] to get the most out of the log-likelihood function. In the next iteration, the log-likelihood function is optimized based on the distributed diffuse scattering parameters θ_{dan} and specular path parameters θ_{sp}. The global iterations for the estimates $\theta_{\text{sp},n}$ and $\theta_{\text{dan},n}$ and shown in (9)–(11) at the bottom of the page, where $n + 1$

$$\hat{\theta}_{\text{sp},n+1} = \underset{\theta_{\text{sp}}}{\arg\min}((x - s(\theta_{\text{sp}}))^H R^{-1}(\hat{\theta}_{\text{dan},n})(x - s(\theta_{\text{sp}}))), \qquad (9)$$

$$\hat{\theta}_{\text{dan},n+1} = \underset{\theta_{\text{dan}}}{\arg\min}((-\ln(\det(R(\theta_{\text{dan}}))) - z_n^H R^{-1}(\theta_{\text{dan}})\hat{z}_n)), \qquad (10)$$

where

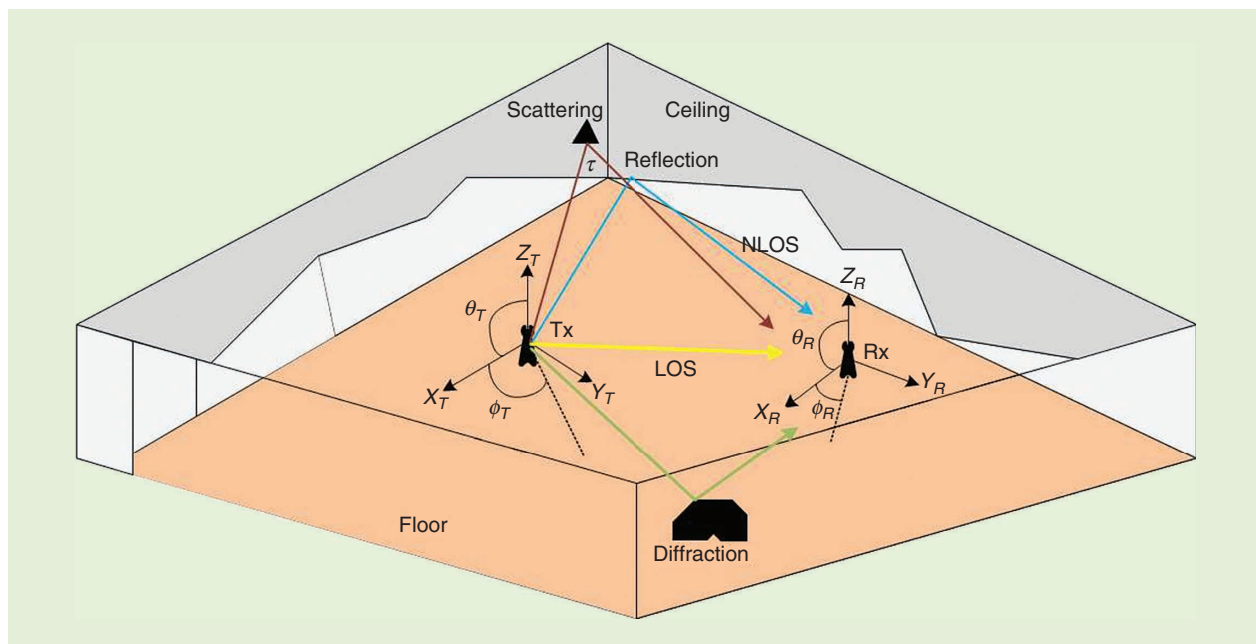$$z_n = x - s(\hat{\theta}_{\text{sp},n+1}). \qquad (11)$$

FIGURE 1. The basic propagation phenomena in a confined environment. NLOS: non-LOS.

represents the "next iteration." For the optimization of parameter θ_{dan} in (10), we employ the algorithm illustrated in [7]. To optimize the parameter θ_{sp} in (9), the parameter estimation method, which includes the R-dimensional unitary estimation of signal parameters via rotational invariant techniques (ESPRIT), SAGE-based channel parameter estimation algorithm, and a gradient based algorithm, may be used [7].

MEASUREMENT AND SETUP CONFIGURATION

MEASUREMENT SCENARIO DESCRIPTION

To conduct a measurement campaign, we considered the underground metro line 7 between Qihua Road and Shanghai University Station in Shanghai, China. The tunnel has an arched cross section with a 2.78-m radius, 3.4-m width at the bottom, 5-m height [see Figure 2(a)], and 1,500-m radius of curvature (R) [see Figure 3(a)]. Concrete reinforcement is applied to the tunnel walls, as shown in Figure 2(b). The tunnel is separated into two sections. The first consists of a 28.1-m-long platform with a rectangular cross section of 5.55 m in height. The second has a nonplatform part with an arched cross section and height of 4.96 m. As far as our wideband measurements are concerned, the longest distance between the transmitting and receiving antenna arrays is 800 m, but our measurements are limited to the first 505 m, owing to the subway's hectic schedule.

At the given operating frequency, 91 measurement locations are chosen within this distance. The first 82 are distributed from 10 m to 415 m at uniform intervals of 5 m, while the next nine have a 10-m separation. Figure 2(c) provides an interior view of the tunnel with the Tx antenna array installed close to the wall. The Rx antenna array acting as an access point is placed on the trolley moving along the central rail of the subway. The Tx antenna array is 1.8 m above the platform, which is 1.3 m higher than the ground. By increasing the Rx height to 2.7 m, we reduced the influence that the people performing the measurements had on the signal transmission.

MEASUREMENT SYSTEM

The pseudo-noise (PN) sequence correlation method is employed for the wideband measurements. By using binary
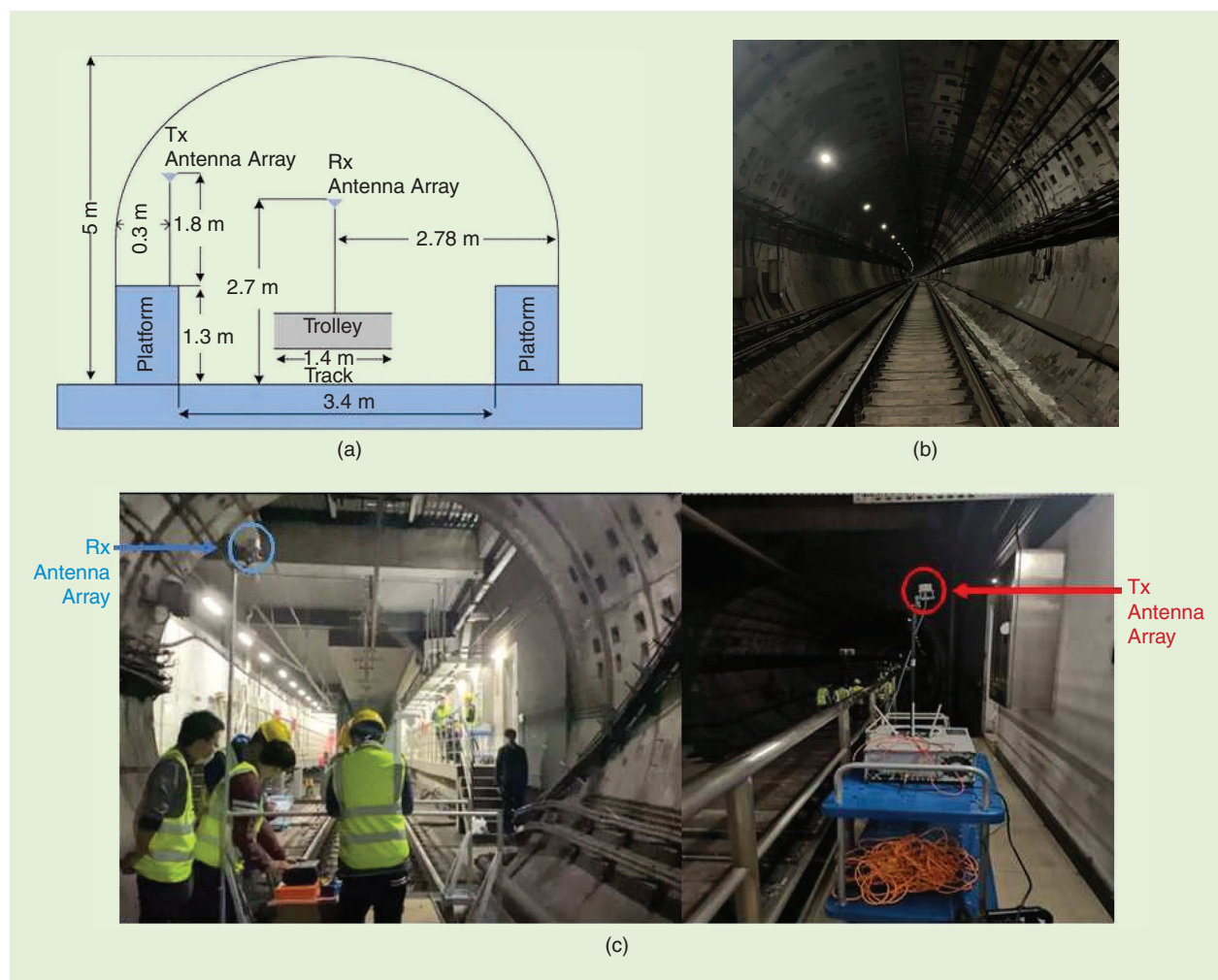

FIGURE 2. The measurement environment: the (a) tunnel cross section, (b) tunnel interior, and (c) measurement scenario, with the Tx antenna array and Rx antenna array locations.

phase-shift keying at the 3.5-GHz carrier frequency, a PN sequence is modulated with a bandwidth of 160 MHz and length of 1,023 chips. To collect data in parallel, the Rx antenna array is divided into eight subchannels. An amplifier is used to enhance the received signal-to-noise ratio (SNR). Notice that static channel measurements of 2,048 (32 × 64) subchannels can be completed in 20 ms, and 128 cycles of measurement data are reported for each receiving antenna location.

A massive MIMO channel sounder system is employed for channel measurements, as depicted in Figure 3(a) and (b). A rubidium clock is used to keep the transceiver antenna arrays synchronized, and 20 dB referenced to 1 mW (dBm) is the total transmitted power. A uniform rectangular antenna patch array (4 × 8) is installed on the Tx antenna array. The receiving side of the uniform cylindrical array is separated into eight sections, and each section has four vertically arranged antenna patches. To achieve one-by-one switching, 64 switching repetitions are performed on the Tx side for each channel sounding cycle. Eight receiving channels' data can be captured at once on the Rx side during a single transmission, requiring only eight switching instances to meet 64 receiving channels. The tunnel is straight for the first 100 m (the LOS path), then curved for the remaining 700 m [the non-LOS (NLOS) path], as described in Figure 3(c).

For channel measurements, directional patch antenna arrays are used at the transmitting and receiving antenna sides. In the horizontal and vertical planes, the 3-dB beamwidth of the antenna elements is 120° and 100°, respectively. In the tunnel, all multipath components can be accurately separated. The Tx and Rx antenna structure is very similar to [18], as documented in Figure 4. In this system, the antenna patches are separated by 0.5 λ, and every antenna pair is composed of two colocated bipolarized antennas (horizontal and vertical). There exist two elements for both antenna patches, each of which has a polarization angle of ±45°. A summary of the important measurement parameters is provided in Table 1.

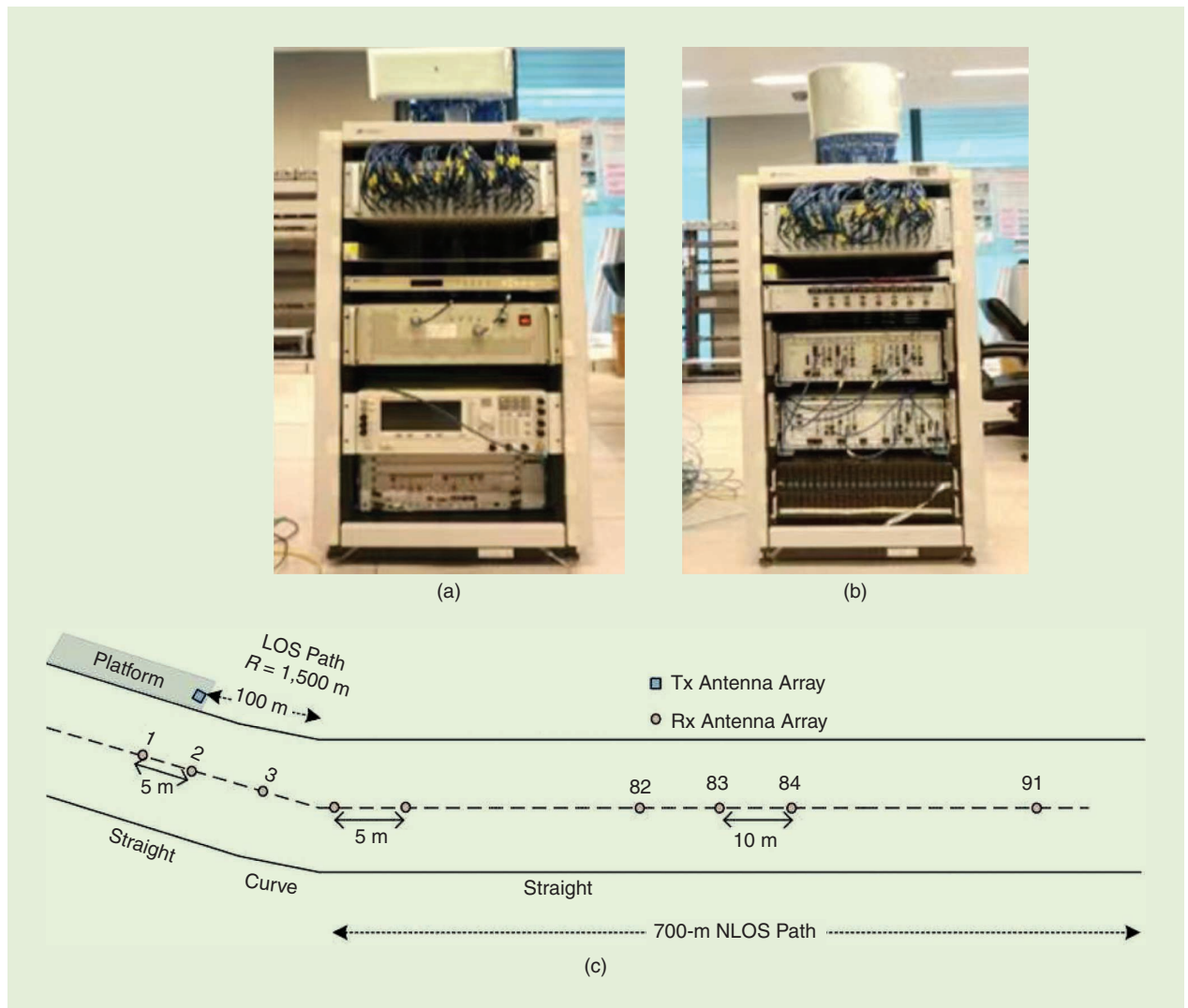**FIGURE 3.** The channel sounder system: the (a) Tx, (b) Rx, and (c) tunnel LOS and NLOS area.

RESULTS AND ANALYSIS

PDP AND DS

The PDP is generally employed to analyze the distribution of multipath components into the delay domain. By averaging the PDP information across the transmitting-to-receiving antenna links, the SSF interference with the effective signal multipaths can be reduced [9], so the average PDP (APDP) is described as

$$\text{APDP}(\tau) = \frac{1}{N_T N_R} \sum_{n=1}^{N_T} \sum_{m=1}^{N_R} |h_{nm}(\tau)|^2, \quad (12)$$

where $h_{nm}(\tau)$ represents the complex CIR between the mth Rx and nth Tx, and N_T and N_R indicate the number of elements in the transmitting and receiving antenna arrays, respectively. We divided our measurements into four scenarios based on the antenna polarization schemes (HH, HV, VH, and VV). In Figure 5, the normalized APDP is shown for the 91 measurement locations. Here, HH polarization means the transmitting and receiving antenna arrays are horizontally polarized, HV means the Tx antenna array is horizontally polarized and Rx antenna array is vertically polarized, VH means the Tx antenna array is vertically polarized and Rx antenna array is horizontally polarized, and VV means the transmitting and receiving antenna arrays are vertically polarized.

The multipath components in the APDP at 3.5 GHz decay quickly with time. With a power threshold of –20 dB, the multipath components attenuate rapidly from 100 ns to 50 ns when the distance between the transmitting and receiving antenna arrays increases. The APDP can be further used to investigate the DS characteristics of a massive MIMO channel. The statistical representation of the delay (τ) in the multipath channel is defined through the DS, which determines the maximum transmission rate, without intersymbol interference in wideband communications. A DS is generally regarded as the second-order moment of the APDP, given by [19], see (13) at the bottom of the page, where τ_k and $P(\tau_k)$ represent the relative delay and estimated power of the kth

multipath while k shows the effective multipath number.

From Figure 6(a), it appears that the DS decreases as the distance between the transmitting and receiving antenna arrays increases, which agrees with the findings of the ray-tracing method in [20]. The empirical cumulative distribution function (CDF) of the RMS DS is provided in Figure 6(b). A modal theory can explain this quite convincingly [21]. Multiple propagation modes are triggered at shorter Tx–Rx distances. At a longer ones, most notably in the case of the NLOS propagation environment, the high-order model attenuation becomes crucial, and only the low-order primary model is

retained. As a result, the RMS DS for the reflected environment is comparatively stable and varies steadily. A lower PL exponent is found in the subway at the given frequency band, but the tunnel still exhibits the waveguide effect. Additionally, the shorter wavelength (λ) of a signal enhances the specular reflections, which further increase the waveguide effect in the tunnel for higher-frequency signals. This waveguide effect can be greatly reduced when the tunnel walls obstruct the multipath components.

There exists a small number of PL exponents in the NLOS region, due to the 1,500-m radius of the curvature. Moreover, it can be seen that the
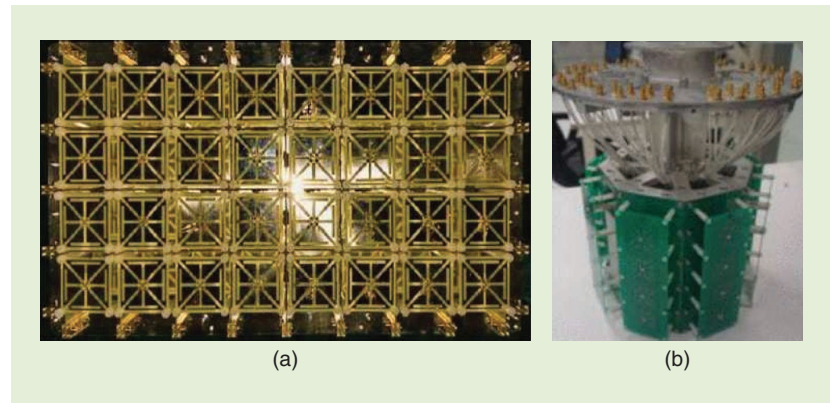

FIGURE 4. The antenna arrays considered for the measurement campaign: the (a) Tx antenna array and (b) Rx antenna array.

TABLE 1. THE MEASUREMENT PARAMETERS.

Parameter	Description
SNR	20 dB
Frequency	3.5 GHz
Bandwidth	160 MHz
Transmitted power	20 dBm
Polarization	Horizontal/vertical
Antenna structure	Uniform rectangular array (Tx antenna array)/ uniform cylindrical array (Rx antenna array)
Tunnel dimensions	5.56 m (width) × 5 m (height) × 800 m (length)
Number of sampling locations	91
Probe signal	PN sequence
Tx/Rx antenna height	1.8 m/2.7 m

$$\tau_{\text{rms}}(d) = \sqrt{\frac{\sum_{k=1}^{K} P(\tau_k) \cdot (\tau_k)^2}{\sum_{k=1}^{K} P(\tau_k)} - \left[\frac{\sum_{k=1}^{K} P(\tau_k) \cdot (\tau_k)}{\sum_{k=1}^{K} P(\tau_k)}\right]^2}, \quad (13)$$
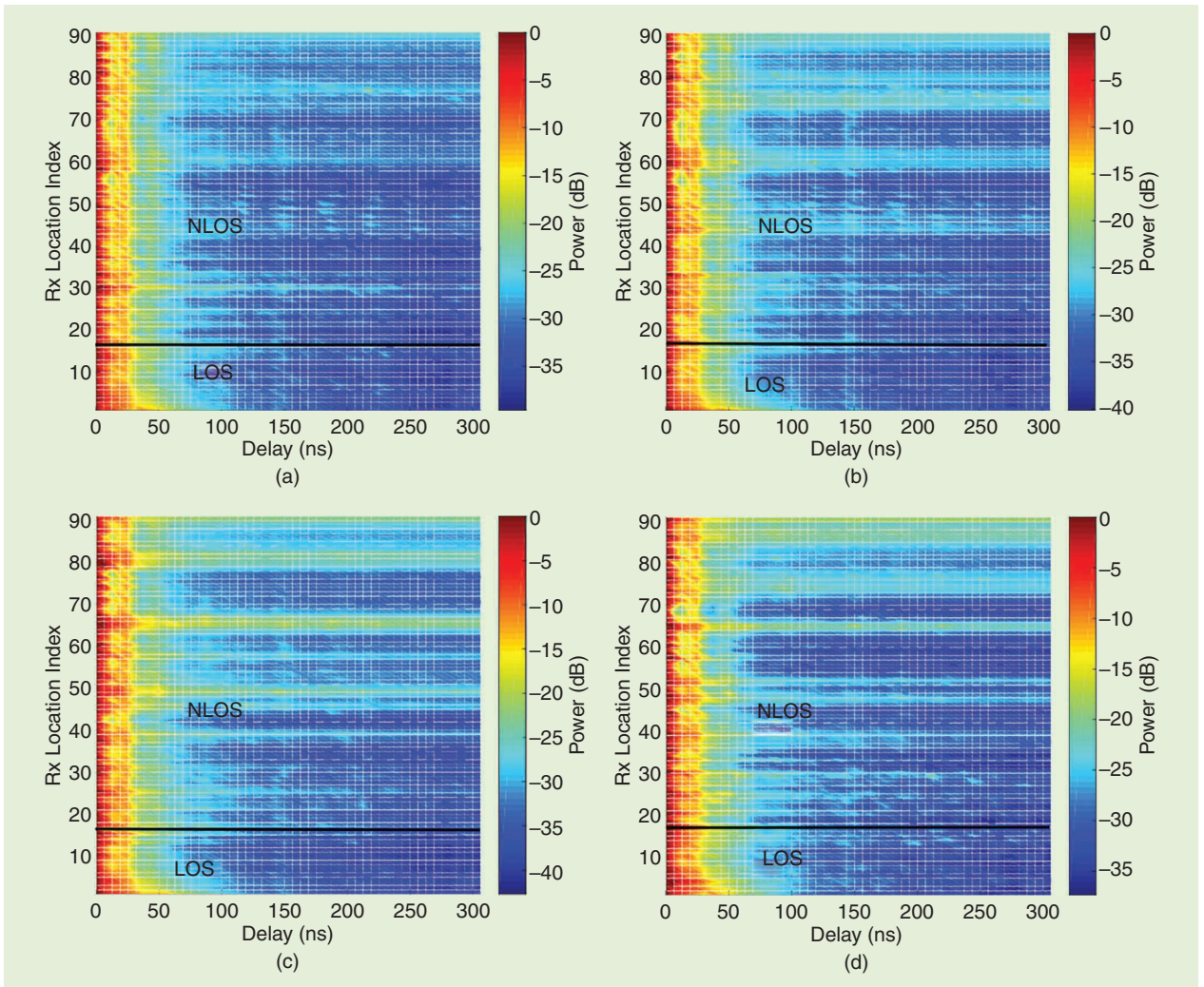
FIGURE 5. The normalized APDP of the effective multipaths for massive MIMO at 3.5 GHz: the (a) *HH* polarized case, (b) *HV* polarized case, (c) *VH* polarized case, and (d) *VV* polarized case.
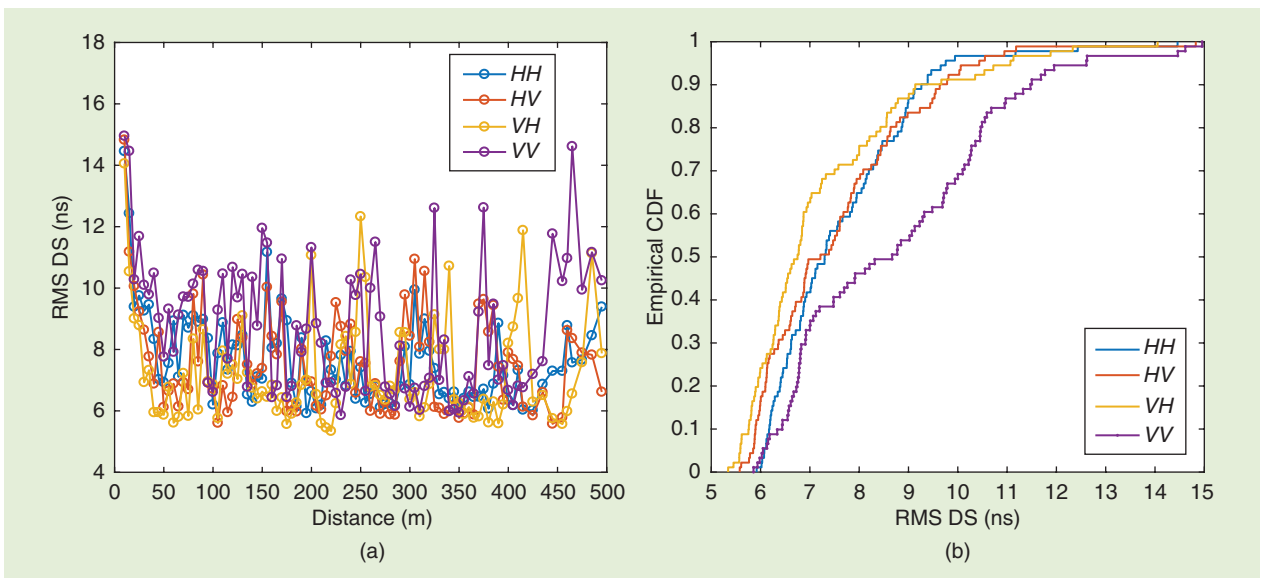

FIGURE 6. The RMS DS of a massive MIMO channel: the (a) variations trend at different receiving antenna locations and (b) cumulative distribution function (CDF).

given results show significant improvement compared to the other MIMO channels in the tunnel [22]. The presence of metallic doors, the uneven tunnel structure (arches and rectangles), and the absence of sidewall smoothness in [22] cause additional reflections before multipath signals can be received at the Rx, resulting in a greater path difference between multipath signals and a rising RMS DS. Table 2 furnishes statistics and percentiles of the RMS DS. At 3.5 GHz, the RMS DS varies from 5.75 ns to 11.51 ns, with the exception of short Tx–Rx distances, for the four antenna polarization schemes.

DMC CHARACTERISTICS IN FREQUENCY, TIME, AND ANGULAR DOMAINS

The power of different multipath components arriving at the Rx during a time interval is mostly influenced by the attenuation factor of free space. As a result, we may presume that one delay bin of the CIR describes a time period of $1/(M_f \times f_c)$, which includes the summation of several propagation paths induced by distributed scattering. On the other hand, the spatial distribution of these propagative multipaths results from significant changes in their path lengths. In Figure 7(a) and (b),

TABLE 2. THE RMS-DS STATISTICS.

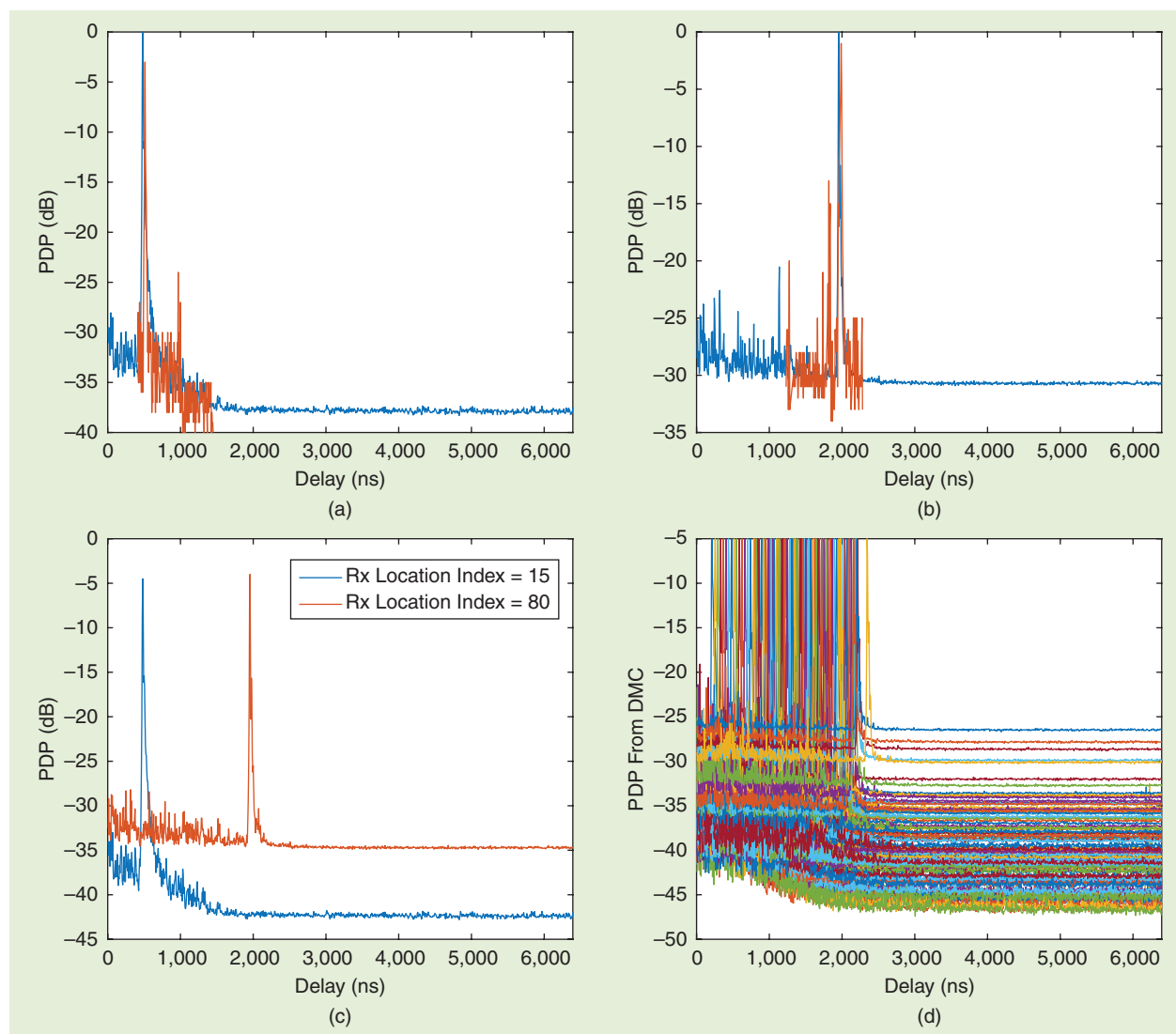| Polarization	10% (ns)	45% (ns)	90% (ns)	Mean (ns)	Standard Deviation (ns)
HH	6.17	7.15	9.26	7.63	1.46
HV	5.89	6.88	9.63	7.54	1.61
VH	5.75	6.51	9.14	7.24	1.7
VV	6.34	7.7	11.47	8.74	2.17

FIGURE 7. For the *HH* polarization case, the reconstructed PDP of the specular paths for the (a) 15th measurement at the (b) 80th measurement location. In the time delay domain, the channel observation after removing the estimated contributions from the specular propagation paths and the estimated PDP from the DMCs for (c) the 15th and 80th measurement locations and (d) all 91 locations.

the PDPs of the 15th (80 m) and 80th (405 m) measurement locations are calculated to distinguish each site response under the *HH* polarization scheme. The PDP recreated from the parameter estimation of the SMCs' propagation paths (θ_{sp}) is included in the same figure. Figure 7(c) represents the PDP after the specular propagation paths $[x - s(\theta)]$ are removed. For the same polarization case, Figure 7(d) gives the estimated PDP of the diffuse components for all measurement locations (1–91) in the τ domain. The observed and estimated PDPs of the DMCs are well matched.

It is also crucial that this PDP no longer has a dominant propagation path. On the other hand, it looks like a dense stochastic effect. Therefore, the contribution of the diffuse scattering to the CIR is considered the dense multipath. Due to space considerations, we do not discuss the other polarization schemes (*HV*, *VH*, and *VV*).

In Figure 8, the variations of α_i, β_{dmc}, τ_{dmc}, μ_R, and μ_T in the frequency, time, and angular domains for the DMCs' propagation parameters under different polarization combinations are shown. Here, α_i is normalized by the highest power gain of different paths

[see Figure 8(a)]. The frequency-domain characteristics are nearly constant for the *HH*, *HV*, and *VH* polarizations in accordance to the distance in the NLOS scenario. It can be seen that α_i decreases with longer distances, and the *HH* polarization has the lowest standard deviation and highest power gain, while the *VV* polarization has the smallest power gain. Moreover, β_{dmc} in Figure 8(b) is about 22 MHz and 24 MHz for the *HH* and *VH* polarizations, respectively. In Figure 8(c) and (d), τ_{dmc}, μ_R, and μ_T represent the peak positions of the DMCs in the delay and angular
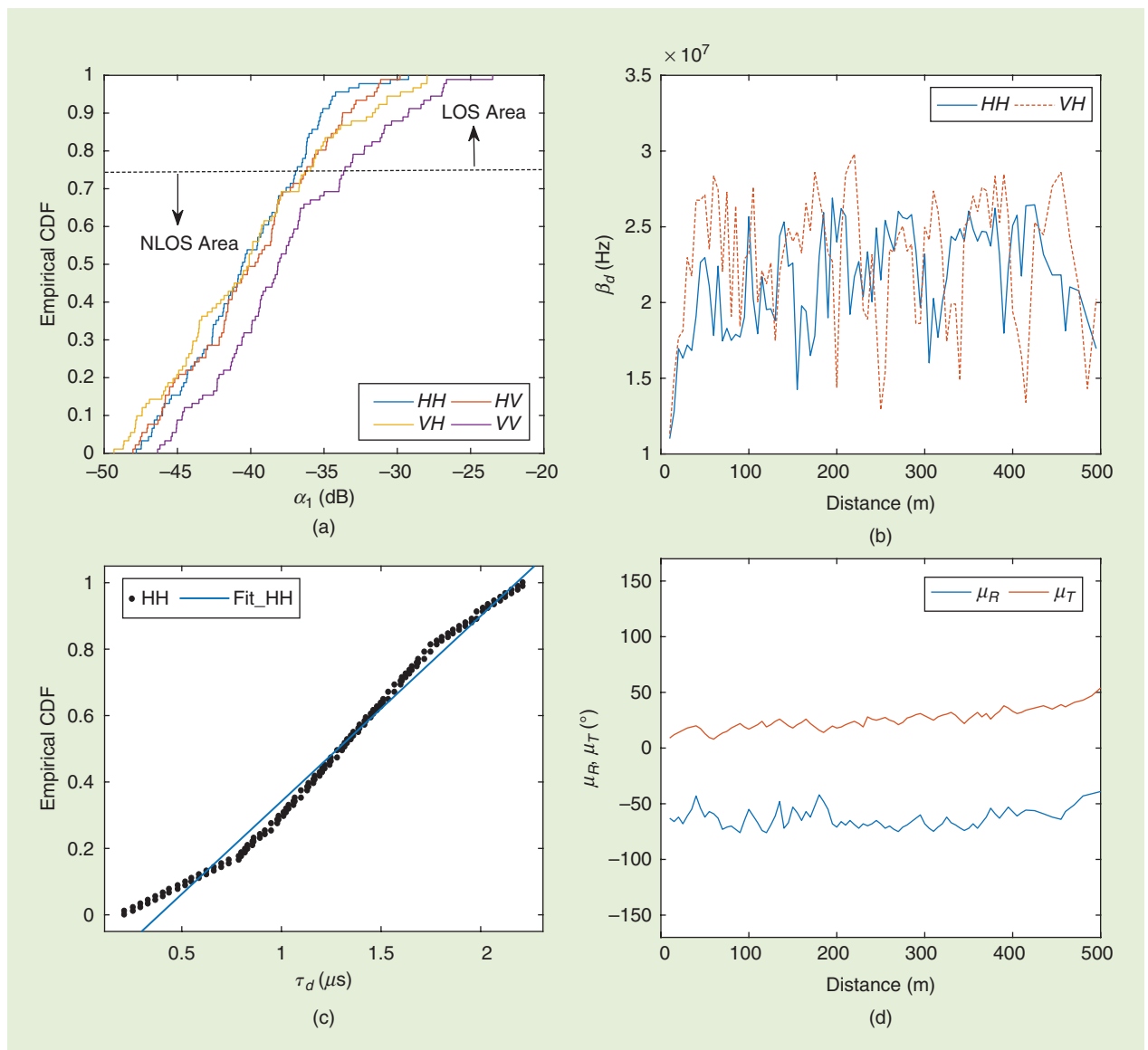

FIGURE 8. The frequency-domain DMC parameter response with respect to distance in the tunnel. (a) The maximum DMC power CDF values for the *HH*, *HV*, *VH*, *VV* polarizations. (b) The DMCs' coherence bandwidth for the *HH* and *VH* polarizations. (c) The DMCs' base time delay for the *HH* polarization with curve fitting. (d) The μ_R and μ_T for the HH polarization.

domains, respectively. The base time delay for DMCs varies between 0.13 and 2.45 μs for HH polarization [see Figure 8(c)]. The results in Figure 8(d) demonstrate that the variations of μ_R and μ_T are around –66° and 18° for the HH polarization.

These results also show that the scattering from the sidewalls between the transmitting and receiving antenna arrays is one of the substantial sources of diffuse scattering. The covariance matrix relationship with the coherence bandwidth and separating distance for different polarization combinations is available in Figure 9. Because of the Toeplitz structure, the covariance matrix has a fairly simple structure in the frequency domain. It can be observed that the VV polarization has maximum variance, while HH has the least. Moreover,

VV is comparatively more influenced by the separating distance, while HH has the least influence.

The cross-polarization ratio (XPR) and copolarization ratio (CPR) for DMC path weights are calculated from the DMCs' path weights as follows [23], [24]:

$$XPR = 10\log_{10}\left(\frac{|\gamma_{d,HH}|^2}{|\gamma_{d,HV}|^2}\right), \quad (14)$$

and

$$CPR = 10\log_{10}\left(\frac{|\gamma_{d,HH}|^2}{|\gamma_{d,VV}|^2}\right), \quad (15)$$

where $\gamma_{d,HH}, \gamma_{d,HV}$, and $\gamma_{d,VV}$ are the path weights for the HH, HV, VH, and VV polarizations. The average DMCs' XPR is roughly 2.1–8.9 dB in our channel, which is 5–6 dB higher than the CPR [see Figure 10(a)]. In contrast to the RiMAX model [7], the DMCs have strong polarization dependences. The estimated XPR is usually a few decibels lower than the DMCs' XPR in [24]. The greater DMC XPR in [24] is mostly due to the diffuse scattering from the ceiling, floor, and walls of the room as well as the existence of dispersed surfaces in the confined environment. Since

$$PL[\text{dB}] = \begin{cases} PL(d_0) + 10n_1\log_{10}(d/d_0) + X_{\sigma 1} & d \leq d_{\text{bp}} \\ PL(d_{\text{bp}}) + 10n_2\log_{10}(d/d_{\text{bp}}) + X_{\sigma 2} & d > d_{\text{bp}} \end{cases}. \quad (17)$$
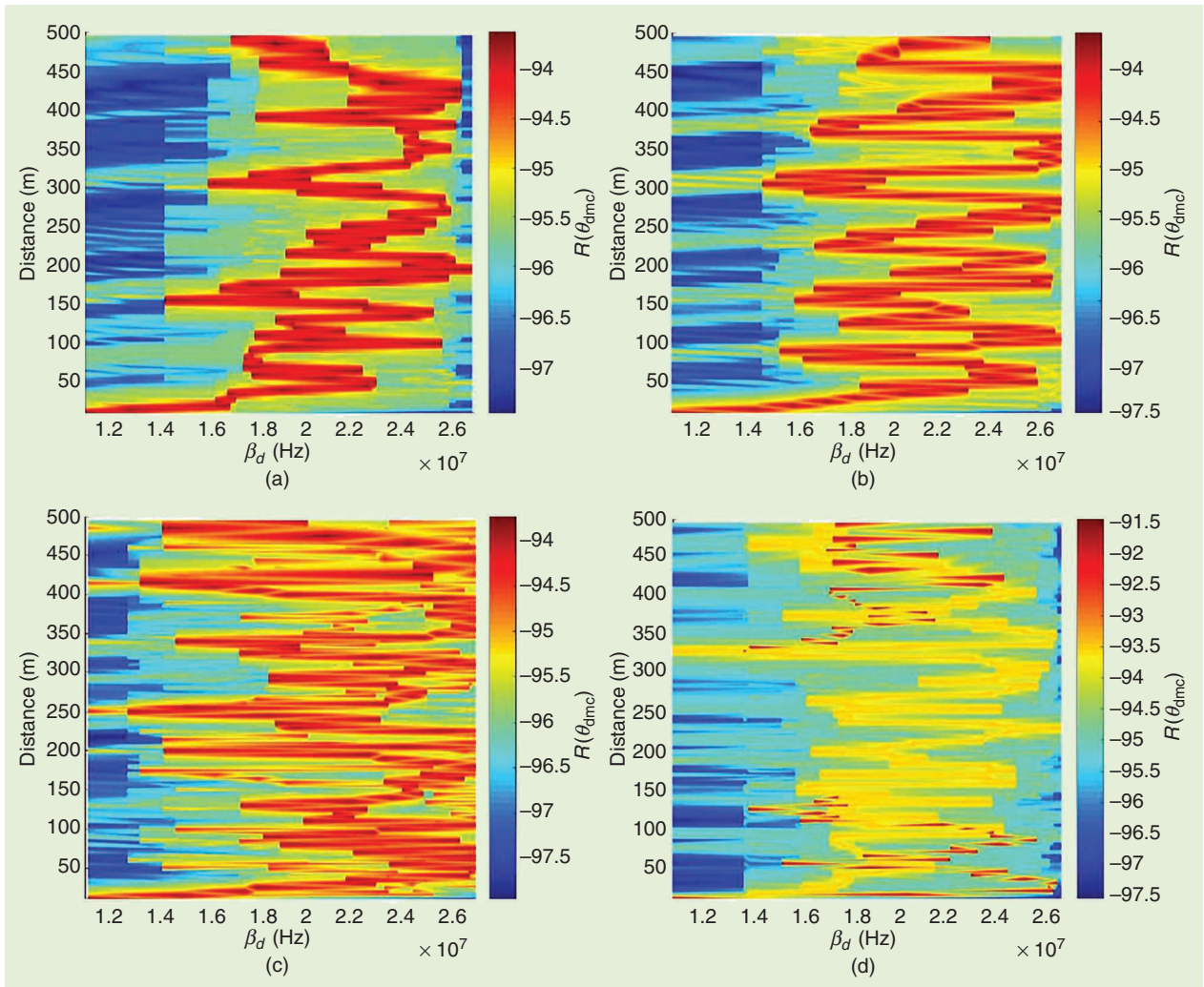

FIGURE 9. The covariance matrix for the (a) *HH*, (b) *HV*, (c) *VH*, and (d) *VV* polarizations.

the dispersed surfaces are virtually horizontal or vertical, the polarization planes of the scattered waves are not considerably changed. In Figure 10(b), the CDF values of the DMCs' power ratios are given for four polarizations. It can be seen that as the distance increases, the power of the DMCs decreases. The DMCs in the *HH* case have the maximum power ratio, while for *VV*, they have the lowest. Moreover, the DMCs have greater power ratios in the LOS scenario than in the NLOS one for all polarizations.

PL AND CHANNEL CAPACITY

PL refers to the signal energy attenuation that occurs after a signal has been transmitted. Figure 11(a) provides the PL measurement results at 3.5 GHz in the subway tunnel. To quantify the PL parameters, the most common model is that employed first in [19]:

$$PL[dB] = PL(d_0) + 10n \log_{10}(d/d_0) + X_\sigma, \quad (16)$$

where d is the separation between the transceiver antennas; d_0 is the reference distance, normally set to 1 m in the tunnel; n is a PL index, which is two in the free space; and X_σ is regarded as a random variable having a Gaussian distribution with a zero mean and a standard deviation of σ. To reduce the mean square error for real measurements and the model, the PL index n is used. The extracted parameters are listed in Table 3. It can be seen that the PL exponent increases with distance, and it is found to be less than that of the free-space radio channel for all polarizations in the tunnel. This is due to the waveguide effect, which remains important. Moreover, the smaller the signals' wavelength, the greater the influence of the SMCs on the tunnel, which increases the

structure's waveguide impact on higher-frequency signals.

Meanwhile, because the curved tunnel wall might interfere with LOS propagation, the position where the LOS (direct) components are obstructed might be critical for precisely predicting the PL at longer distances [25]. We estimated 91 m as a transition point (d_{bp}) for the tunnel LOS and NLOS propagations, based on a geometric characterization of the structure. In the tunnel, the two-slope PL model may be described as [25] [see (17) at the bottom of the previous page].

Figure 11(b)–(e) represents the two-slope PL model for the *HH*, *HV*, *VH*, and *VV* polarizations at 3.5 GHz, respectively. Table 4 contains the model coefficients for the polarization schemes. In the LOS propagation environment, the PL exponent ranges from 1.48 to 1.8, whereas in the NLOS
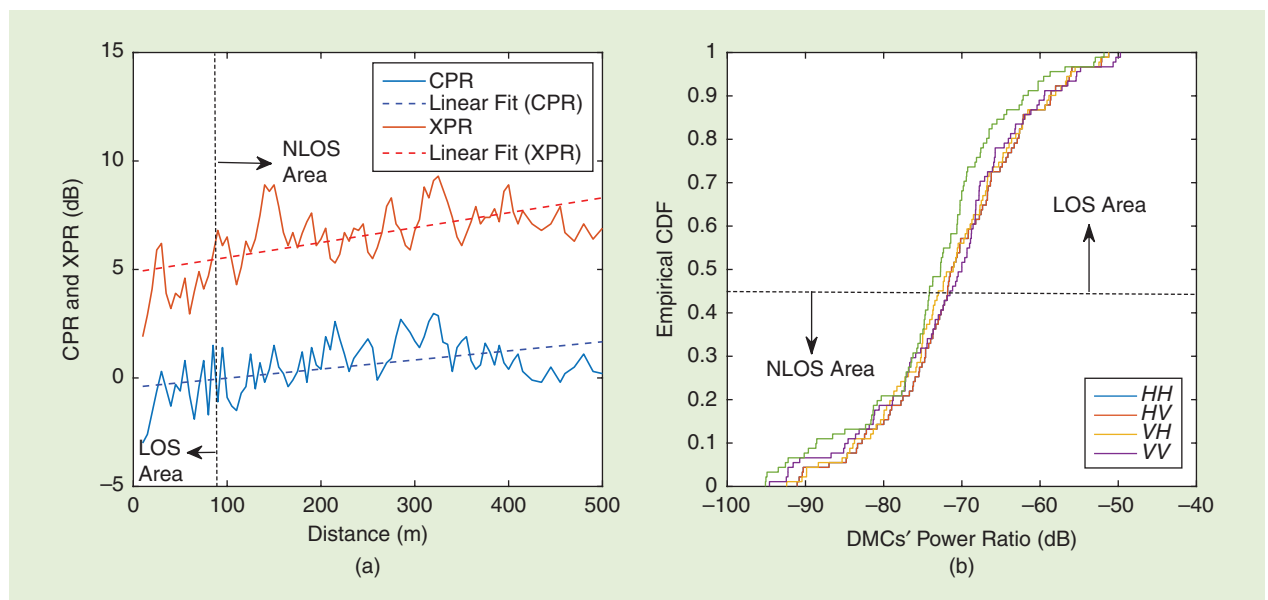

FIGURE 10. The DMC characteristics: the (a) CPR and XPR versus the path weight variations and (b) DMCs' power ratio for the *HH*, *HV*, *VH*, and *VV* polarizations.

TABLE 3. THE PL COEFFICIENTS.

Polarization	$PL(d_0)$(dB)	n	σ (dB)
HH	40.56	1.57	6.9
HV	39.41	1.65	6.88
VH	33.71	1.9	6.81
VV	39.02	1.76	6.82

TABLE 4. THE COEFFICIENTS OF THE TWO-SLOPE PL MODEL.

Polarization	LOS			NLOS		
	$PL(d_0)$	n_1	σ_1 (dB)	$PL(d_{bp})$ (dB)	n_2	σ_2 (dB)
HH	42.36	1.48	4.84	71.3	1.79	7.31
HV	40.34	1.55	4.69	70.56	1.92	7.3
VH	34.82	1.8	4.52	70.01	2.47	7.23
VV	40.01	1.67	4.9	72.58	2.34	7.19

environment, the PL exponent goes from 1.79 to 2.47. This demonstrates that the multipath signals propagate along the axial route of the tunnel and via reflection between the walls before reaching the break point, resulting in a lower propagation loss. The aforementioned waveguide effect is decreased when the sidewall of the curved tunnel obstructs the multipath components. Since the 1,500-m radius of curvature in our model is substantially larger than that of [25], the proposed channel model has a smaller PL exponent in the NLOS area than the PL models do in [25].
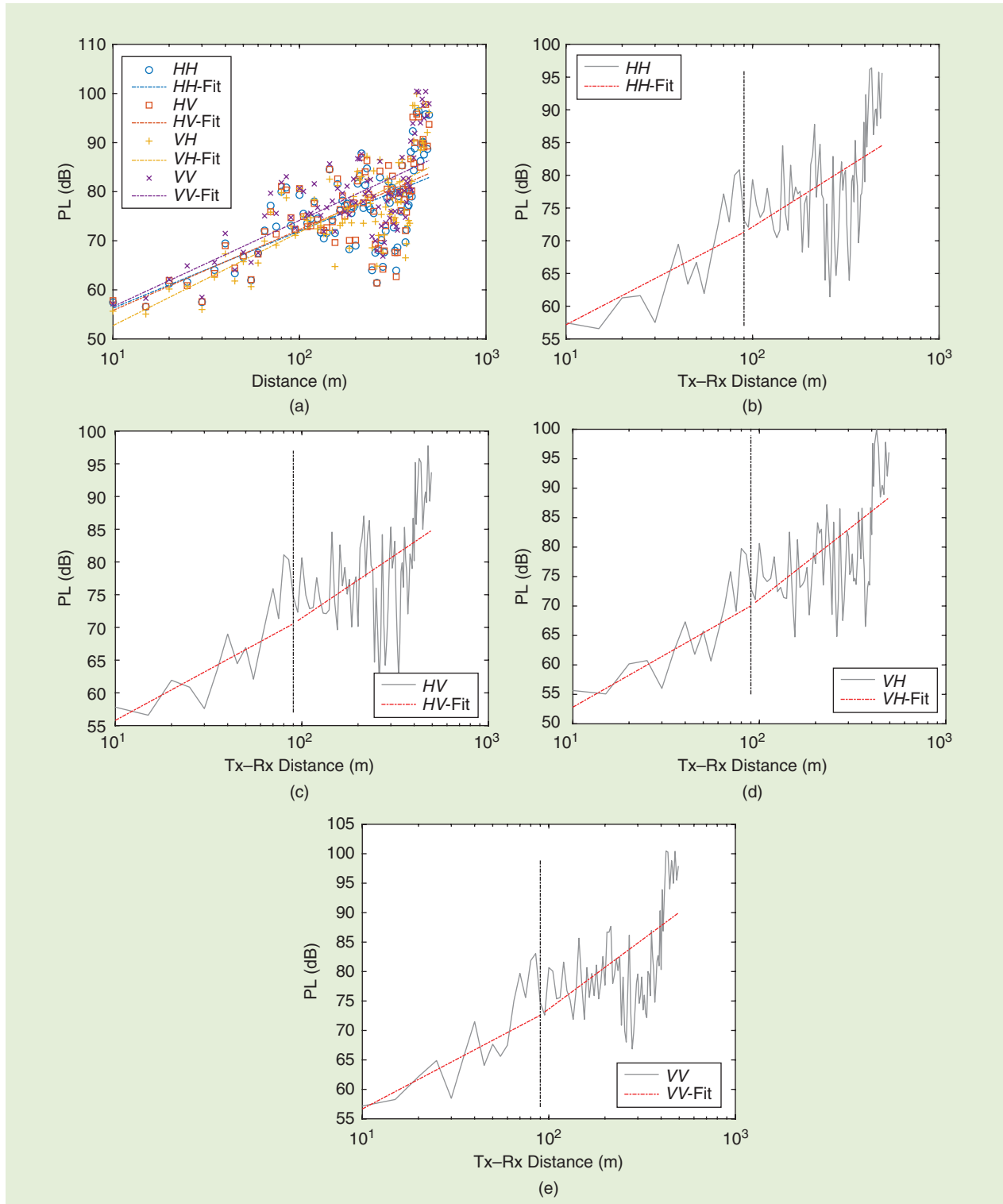
FIGURE 11. The PL model for (a) the *HH*, *HV*, *VH*, and *VV* polarizations. The measured data comparison with a two-slope PL model for the (b) *HH*, (c) *HV*, (d) *VH*, and (e) *VV* polarizations.

Moreover, the Tx antenna array in our measurements is near the tunnel sidewall, but the Tx and Rx in [25] are placed along the tunnels' middle part. Among the four propagation schemes, the propagation attenuation rate of the HH polarization is found to be the least in the LOS and NLOS situations when compared to the others.

The Bartlett technique is used to compute the angular spread of the HH and HV transceivers. The mathematical relationship for calculating the angular spread is given in [26]:

$$\theta_{AS} = \sqrt{\frac{\sum_{i=1}^{N} P_i (\theta_i - \bar{\theta})^2}{P}}, \quad (18)$$

and

$$\bar{\theta} = \frac{\sum_{i=1}^{N} P_i \theta_i}{P}, \quad (19)$$

where P is the total received power at a given measurement location, and θ_i and P_i are the direction of arrival/departure and power of the ith path, respectively. In Figure 12, the angular distributions of the azimuth angle-of-departure (AoD), elevation angle-of-departure (EoD), azimuth angle of arrival (AoA), and elevation angle of arrival (EoA) for each receiving antenna site are shown for different receiving antenna locations. Moreover, the

statistical characteristics of the angular spread values for AoD, EoD, AoA, and EoA for the HH, HV, VH, and VV polarizations are given in Table 5. It can be seen than when the distance between the transmitting and receiving antennas grows, the angular spread decreases dramatically. The AoA and EoD of the HH and HV antennas are found to be within 25°.

The EoD of the HV antenna arrays is greater than that of the HH antenna arrays when the transceiver distance is between 180 m and 470 m. The reason is that multipath signals must be reflected more times in the curved section of the tunnel before reaching the Rx, causing the angular spread values to increase. The EoD and EoA

of HH and HV are all within 17°. The AoA and AoD for HH and HV decline when the transceiver distance is shorter than 100 m, where HH is found to be smaller than HV. The EoD and EoA of the HV and HH signals finally become the same when the distance between the Tx and Rx exceeds 100 m. They are practically the same until the transceiver distance reaches 180 m. It can be observed that the curvature radius of the tunnel has a greater influence on the azimuth angular spread than on the elevation angular spread.

To visualize additional characteristics of the measured data, spatial correlation coefficients are considered. When the normalized AoA is ϕ_o and the normalized separation is given as $D = 2\pi d/\lambda$, where d is the separation distance between the transmitting and receiving antenna arrays, the spatial correlation coefficients can be calculated using the following relationship [27]:

$$\rho_c(D) = R_{XX}(D) + jR_{XY}(D), \quad (20)$$

where [see (21) and (22) at the bottom of the page] $J_m(*)$ is the first kind of Bessel function of the mth order, σ is the angular spread, and $\Delta\varphi$ is uniformly distributed between $-\pi$ and $+\pi$.

We considered the Rx antenna array at a distance of 80 m from the starting point in the tunnel. Figure 13 conveys the spatial correlation coefficients for four combinations of vertically and horizontally polarized antenna arrays. The vertical polarization coefficient increases as the incidence angle grows. However, the vertical polarization coefficient has a greater Brewster angle

$$R_{XX}(D) = J_0(D) + Q \sum_{m=1}^{\infty} J_{2m}(D) e^{-2\sigma^2 m^2} \cos(2m\varphi_0)$$
$$\times \left[\text{erf}\left(\frac{\Delta\varphi}{\sigma\sqrt{2}} - jm\sigma\sqrt{2}\right) - \text{erf}\left(-\frac{\Delta\varphi}{\sigma\sqrt{2}} - jm\sigma\sqrt{2}\right) \right] \quad (21)$$

and

$$R_{XY}(D) = Q \sum_{m=1}^{\infty} J_{2m+1}(D) e^{-2\sigma^2(m+1/2)^2} \sin((2m+1)\varphi_0)$$
$$\times \text{Re}\left[\text{erf}\left(\frac{\Delta\varphi}{\sigma\sqrt{2}} - j\sigma\sqrt{2}\left(m + \frac{1}{2}\right)\right) - \text{erf}\left(-\frac{\Delta\varphi}{\sigma\sqrt{2}} - j\sigma\sqrt{2}\left(m + \frac{1}{2}\right)\right) \right], \quad (22)$$
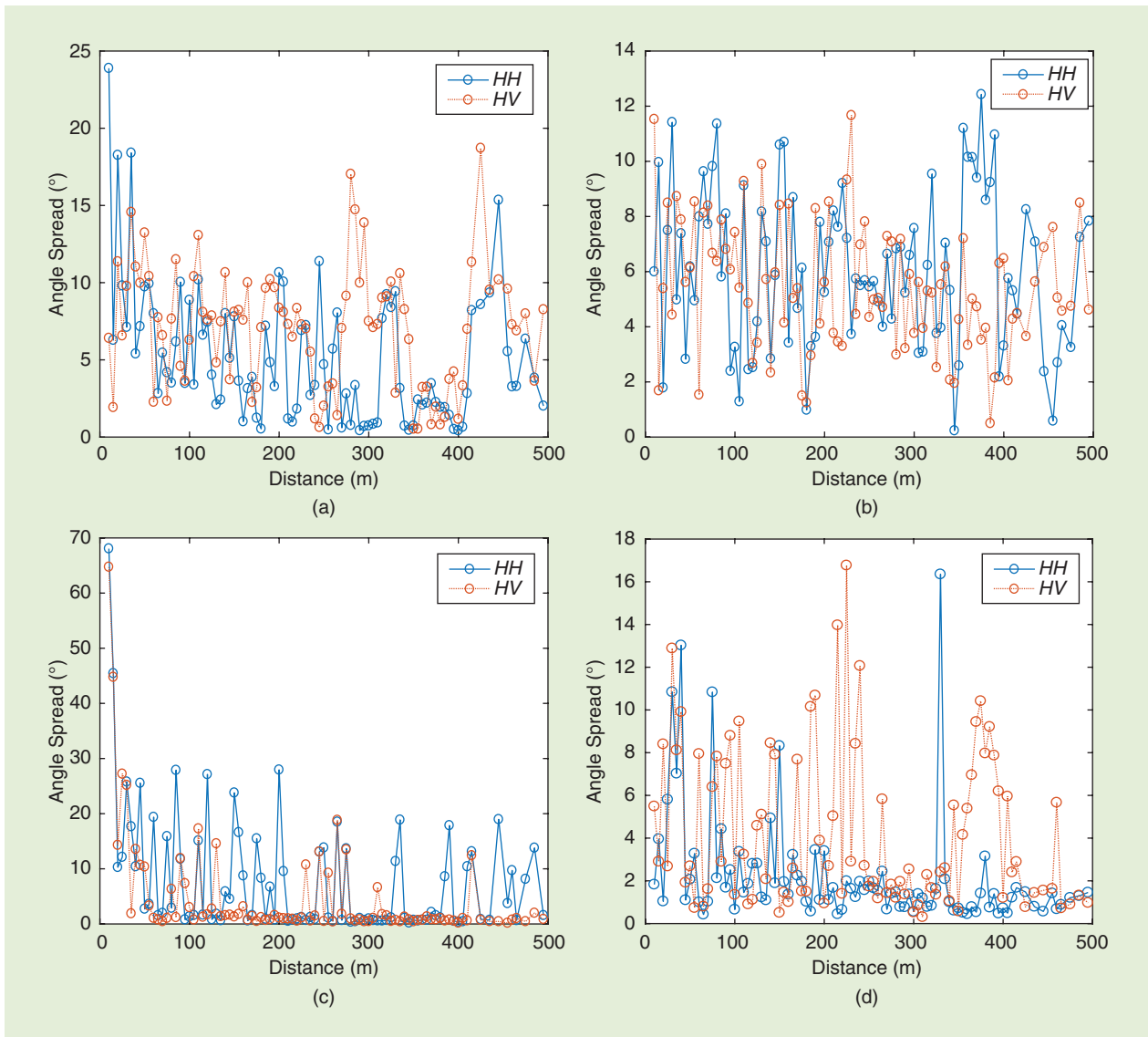
FIGURE 12. The *HH* and *HV* polarized antenna array angular spread at different locations for the (a) angle-of-arrival (AoA), (b) elevation angle-of-arrival (EoA), (c) angle-of-departure (AoD), and (d) elevation angle-of-departure (EoD).

than the horizontal one. In horizontally polarized waves, the incident ray is horizontally polarized along the ceiling and floor of the tunnel, whereas the vertical polarization is detected on the tunnel wall. In the case of vertically polarized waves, the opposite case will be observed. Based on the reflection coefficients, the horizontal polarization has stronger reflected rays than the vertical one. In the tunnel, since the structure's height is less than its width, the reflected signals from the wall have a larger AoA than those from the floor and ceiling. Due to this, the horizontal polarization has a higher angular spread than the vertical one.
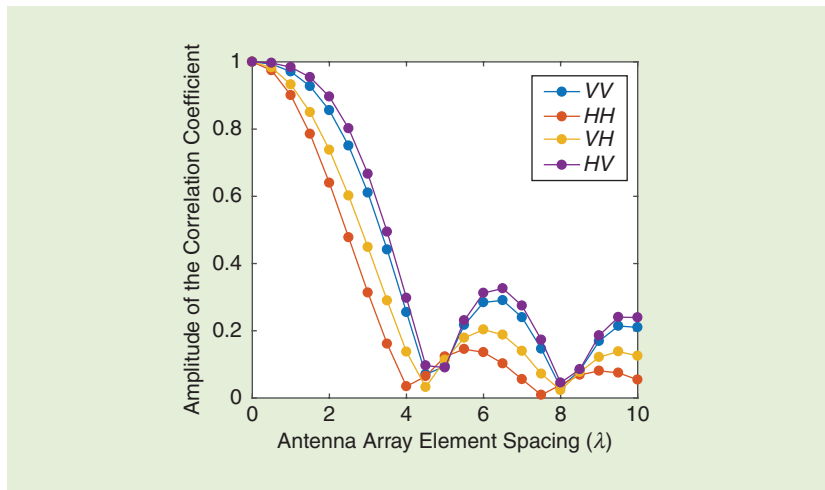

FIGURE 13. The correlation coefficients for different antenna array polarizations.

Accordingly, the vertically polarized layout has lower correlation coefficients than the horizontally polarized configuration. Also, we can see that the spatial correlation coefficient for the *HH* case converges to nearly zero at 7.6 λ when the angular spread is estimated as 30.13°. Therefore, the *HH* polarized transceiver arrays should have a separation distance greater than 7.6 λ to avoid correlation. As evident from the results, the spatial correlation coefficient decreases when the angular spread increases.

Considering, as an example, a configuration where the transmitting and receiving antenna arrays are 20 m apart at 3.5 GHz, there exist only 12 effective eigenvalues in the channel matrix, which is significantly fewer than the smallest value of the transmitting and receiving antenna
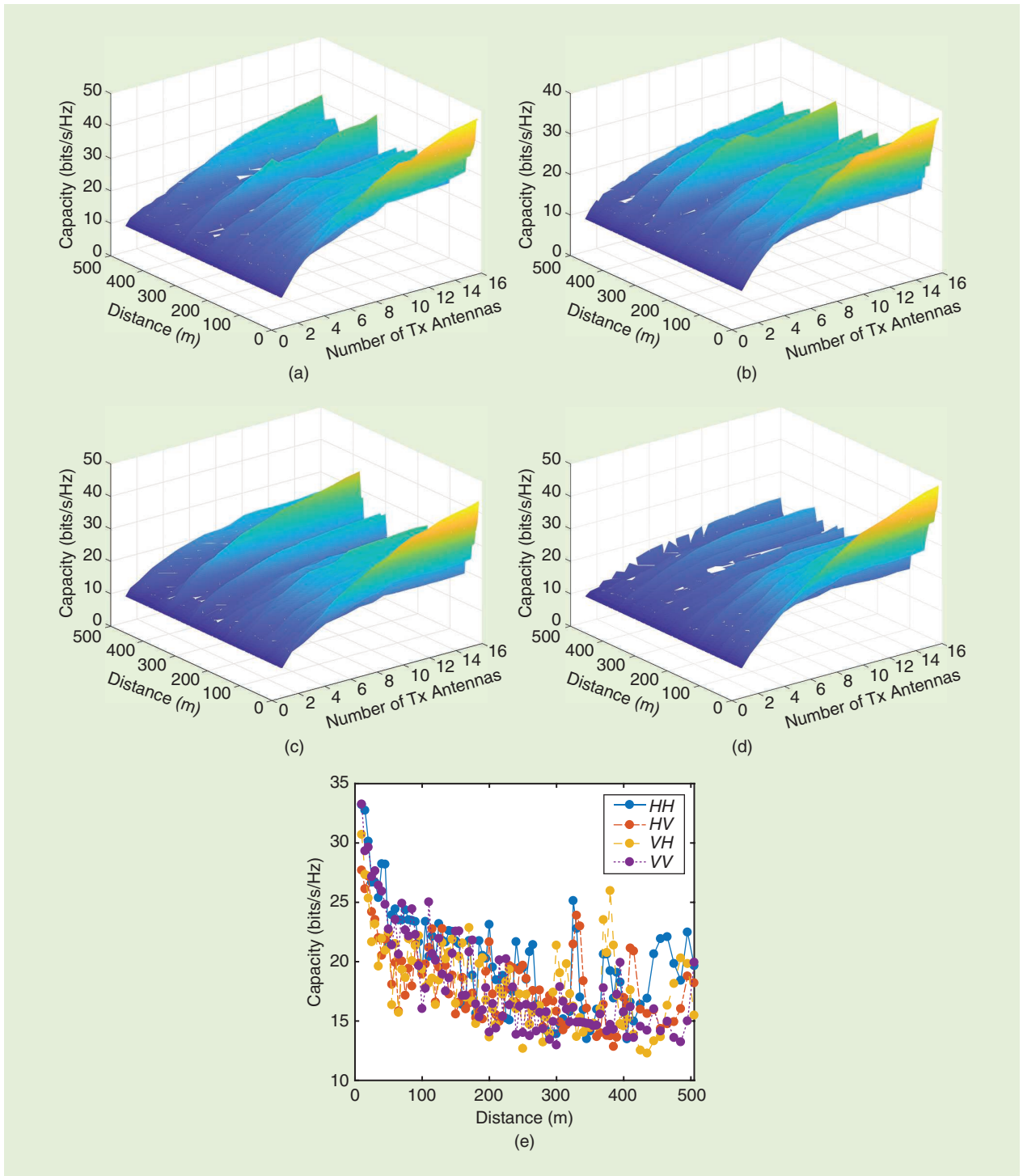

FIGURE 14. The massive MIMO channel capacity for different antenna array polarizations: the (a) *HH*, (b) *HV*, (c) *VH*, (d) *VV*, and (e) channel capacity variations trend according to distance.

elements $[\min(N_T, N_R)]$. This shows that, in the tunnel, the massive MIMO channel matrix will suffer from severe rank reduction, which will adversely affect multistream parallel transmissions. Because the received signal strength changes with the transceiver array locations, channel normalization provides a reasonable comparison between various locations. The normalized channel matrix for channel realization is expressed in the following way [28]:

$$H_{\text{nor}} = H \sqrt{\frac{N_T N_R}{\|H\|_F^2}}, \qquad (23)$$

and

$$\|H\|_F = \sqrt{\sum_{i=1}^{N_R} \sum_{i=1}^{N_T} |h_{ij}|^2}, \qquad (24)$$

where $\|H\|_F$ is the Frobenius Norm.

If no channel state information is provided at the Tx end but is thoroughly acquired at the Rx end, the massive MIMO channel capacity can be estimated as follows [29], [30]:

$$C = \log_2 \det \left[I_{N_R} + \frac{\rho}{N_T} H_{\text{nor}} H_{\text{nor}}^H \right]$$
$$(\text{bits/s/Hz}), \qquad (25)$$

where ρ is the average SNR and I_{NR} is the identity matrix. The channel capacity characteristics for the four polarization schemes are provided in Figure 14(a)–(d) to articulate the capacity response with different sizes of transmitting antenna arrays and at different measurement locations, whereas Figure 14(e) provides a 2D representation of the capacity versus the distance variations. In Figure 14, it is evident that the capacity variations of the *HH* polarized arrays are stable and show significant improvement compared to the other cases. In a tunnel, as the distance between the transmitting and receiving antenna arrays increases, there is a gradual reduction in the distance between the reflected (NLOS) and LOS components, causing less DS. In this regard, the channel diversity gain is less likely to increase when the similarity among components increases. Due to the tunnel curvature, the direct component in the NLOS propagation area will be blocked, and there will be irregular reflections from the structure's walls.

The multipath signal propagation distances are quite stable. Therefore, the massive MIMO channel capacity does not show significant changes with different transceiver distances.

CONCLUSIONS

In this article, we conducted a measurement campaign at the 3.5-GHz frequency band for a 32×64 massive MIMO radio channel in a tunnel. On the basis of the CIRs, the channel delay profile, RMS DS, SMCs, DMCs, PL, angular spread, channel correlation coefficients, and channel capacity were examined for four polarization schemes. A RiMAX-based algorithm was used to compute the specular components and DMCs. The algorithm employed an iterative approach to sequentially optimize the log-likelihood function according to the parameters of the SMC and DMC propagation paths. For future 5G mobile communications in tunnels, railways, and mines, this study will be suitable for numerous applications.

The following conclusions can be drawn:

1) As a result of the tunnel waveguide effect, the RMS DS is limited. Multipath delays within the range of 100 ns are observed, whereas the maximum value for the RMS DS is less than 15 ns.
2) A gradient-based optimization strategy is used to optimize the log-likelihood function of SMC and DMC parameter subsets. In addition, the RiMAX-based algorithm returns a variance estimate of the computed parameters; thus, their accuracy can be optimized.
3) Additionally, we found that even for the same antenna spacing, the spatial correlation coefficient decreases as the angular spread increases.
4) In the tunnel, the channel matrix eigenvalues decline rapidly, and the channel rank is significantly reduced. According to measurements at 3.5 GHz, the maximum capacity value of the massive MIMO radio channel is 33.2 (bits/s/Hz), and the smallest capacity value is 12.4 (bits/s/Hz).
5) The PL exponent increases with distance, while the DS and capacity falls as the distance grows. Moreover, it is observed that the *HH* polarization

configuration for the Tx–Rx antenna arrays performs slightly better than the others.

AUTHOR INFORMATION

Asad Saleem (asadalvi64@yahoo.com) is a postdoctoral fellow at Shenzhen University, Shenzhen, 518060, China. His research interests include wireless communications and channel modeling.

Haixia Cui (cuihaixia@m.scnu.edu.cn) is a full professor at South China Normal University, Guangzhou, 510006, China. Her research interests include cooperative communication, wireless resource allocation, and antennas. She is a Senior Member of IEEE.

Yejun He (yjhe@szu.edu.cn) is a full professor at Shenzhen University, Shenzhen, 518060, China. His research interests include wireless communications, antennas, and radio frequency. He is a Senior Member of IEEE.

Amir Boag (boag@tau.ac.il) is a full professor at Tel Aviv University, Tel Aviv, 69978, Israel. His research interests include computational electromagnetics, wave scattering, imaging, and the design of antennas and optical devices. He is a Fellow of IEEE.

REFERENCES

[1] N. Parchin, H. Basherlou, Y. Al-Yasir, and R. Abd-Alhameed, "A broadband multiple-input multiple-output loop antenna array for 5G cellular communications," *AEU-Int. J. Electron. Commun.*, vol. 127, p. 153,476, Dec. 2020, doi: 10.1016/j.aeue.2020.153476.
[2] G. M. Zebari, D. A. Zebari, and A. Al-Zebari, "Fundamentals of 5G cellular networks: A review," *J. Inform. Technol. Inf.*, vol. 1, no. 1, pp. 1–5, Apr. 2021.
[3] A. Osseiran *et al.*, "Scenarios for 5G mobile and wireless communications: The vision of the METIS project," *IEEE Commun. Mag.*, vol. 52, no. 5, pp. 26–35, May 2014, doi: 10.1109/MCOM.2014.6815890.
[4] M. Novak, A. H. Abdelrahman, H. Yi, L. Piazzi, and Z. Ma, "Tightly coupled dipole array for 5G multi-band cellular base station antennas,"

in *Proc. IEEE Int. Symp. Antennas Propag. North Amer. Radio Sci. Meeting*, Montreal, Canada, pp. 1681–1682, Jul. 2020, doi: 10.1109/IEEECONF35879.2020.9329536.

[5] A. R. Flores, R. C. De Lamare, and B. Clerckx, "Linear precoding and stream combining for rate splitting in multiuser MIMO systems," *IEEE Commun. Lett.*, vol. 24, no. 4, pp. 890–894, Apr. 2020, doi: 10.1109/LCOMM.2020.2969158.

[6] E. Björnson, M. Bengtsson, and B. Ottersten, "Optimal multiuser transmit beamforming: A difficult problem with a simple solution structure," *IEEE Signal Process. Mag.*, vol. 31, no. 4, pp. 142–148, Jul. 2014, doi: 10.1109/MSP.2014.2312183.

[7] A. Richter, "Estimation of radio channel parameters: Models and algorithms," Ph.D. dissertation, Technischen Universitat Ilmenau, Ilmenau, Germany, May 2005.

[8] S. R. Kshetri, E. Tanghe, D. P. Gaillot, M. Lienard, L. Martens, and W. Joseph, "Polarimetrie properties of indoor MIMO channels for different floor levels in a residential house," in *Proc. 11th Eur. Conf. Antennas Propag. (EuCAP)*, Paris, France, May 2017, pp. 2463–2467, doi: 10.23919/EuCAP.2017.7928329.

[9] D. P. Gaillot *et al.*, "Polarization properties of specular and dense multipath components in a large industrial hall," *IEEE Trans. Antennas Propag.*, vol. 63, no. 7, pp. 3219–3228, Jul. 2015, doi: 10.1109/TAP.2015.2430374.

[10] J. Li, B. Ai, R. He, M. Yang, and Z. Zhong, "On modeling of dense multipath component for indoor massive MIMO channels," *IEEE Antennas Wireless Propag. Lett.*, vol. 18, no. 3, pp. 526–530, Mar. 2019, doi: 10.1109/LAWP.2019.2896088.

[11] D. Solomitckii *et al.*, "Characterizing the impact of diffuse scattering in urban millimeter-wave deployments," *IEEE Wireless Commun. Lett.*, vol. 5, no. 4, pp. 432–435, Aug. 2016, doi: 10.1109/LWC.2016.2580669.

[12] A. Saleem, F. Zhang, M. Wang, X. Yin, and G. Zheng, "Proficiency of leaky coaxial cable-based MIMO system using radiated field distribution," *Int. J. Antennas Propag.*, vol. 2018, Dec. 2018, doi: 10.1155/2018/5016847.

[13] A. E. Forooshani, R. D. White, and D. G. Michelson, "Effect of antenna array properties on multiple-input multiple-output system performance in an underground mine," *IET Microw., Antennas Propag.*, vol. 7, no. 13, pp. 1035–1044, Oct. 2013, doi: 10.1049/iet-map.2013.0102.

[14] J. Li *et al.*, "Channel characterization for massive MIMO in subway station environment at 6 GHz and 11 GHz," in *Proc. IEEE 88th Veh. Technol. Conf. (VTCFall)*, Chicago, IL, USA, Aug. 2018, pp. 1–5, doi: 10.1109/VTCFall.2018.8690735.

[15] A. Saleem, M. Wang, G. Zheng, and X. Yin, "Spatial characteristics of wideband channels using leaky coaxial cables in tunnel scenario," *Int. J. Antennas Propag.*, vol. 2019, Article ID 9374905, May 2019, doi: 10.1155/2019/9374905.

[16] F. Challita *et al.*, "On the contribution of dense multipath components in an intrawagon environment for 5G mmW massive MIMO channels," *IEEE Antennas Wireless Propag. Lett.*, vol. 18, no. 12, pp. 2483–2487, Dec. 2019, doi: 10.1109/LAWP.2019.2940831.

[17] T. Choi *et al.*, "Experimental investigation of frequency domain channel extrapolation in massive MIMO systems for zero-feedback FDD," *IEEE Trans. Wireless Commun.*, vol. 20, no. 1, pp. 710–725, Jan. 2021, doi: 10.1109/twc.2020.3028161.

[18] L. Hao *et al.*, "Measurement-based double-directional polarimetric characterization of outdoor massive MIMO propagation channels at 3.5 GHz," in *Proc. IEEE 21st Int. Workshop on Signal Process. Adv. Wireless Commun. (SPAWC)*, Atlanta, GA, USA, May. 2020, pp. 1–5, doi: 10.1109/SPAWC48557.2020.9154274.

[19] A. Goldsmith, *Wireless Communications*. Cambridge, U.K.: Cambridge Univ. Press, Aug. 2005.

[20] A. Saleem, M. Wang, and G. Zheng, "Scattering of electric field from leaky coaxial cable in confined area," *Int. J. Antennas Propag.*, vol. 2017, Oct. 2017, doi: 10.1155/2017/2894397.

[21] D. G. Dudley, M. Lienard, S. F. Mahmoud, and P. Degauque, "Wireless propagation in tunnels," *IEEE Antennas Propag. Mag.*, vol. 49, no. 2, pp. 11–26, Jul. 2007, doi: 10.1109/MAP.2007.376637.

[22] R. Sun *et al.*, "Investigation of MIMO channel characteristics in a two-section tunnel at 1.4725 GHz," *Int. J. Antennas Propag.*, vol. 2017, Article ID 3693149, Jul. 2017, doi: 10.1155/2017/3693149.

[23] Y. Konishi, L. Materum, J.-I. Takada, I. Ida, and Y. Oishi, "Cluster polarization behavior of a MIMO system: Measurement, modeling and statistical validation of the correlation of its channel parameters," in *Proc. IEEE 20th Int. Symp. Personal, Indoor Mobile Radio Commun. (PIMRC)*, Tokyo, Japan, Apr. 2009, pp. 1786–1790, doi: 10.1109/PIMRC.2000.5450178.

[24] K. Saito, J.-I. Takada, and M. Kim, "Characteristics evaluation of dense multipath component in 11GHz-band indoor environment," in *Proc. 10th Eur. Conf. Antennas Propag. (EuCAP)*, Davos, Switzerland, Jun. 2016, pp. 1–3, doi: 10.1109/EuCAP.2016.7481520.

[25] S. K. Kalyankar, Y. H. Lee, and Y. S. Meng, "Two-slope path loss model for curved-tunnel environment with concept of break point," *IEEE Trans. Intell. Transp. Syst.*, vol. 22, no. 12, pp. 7850–7859, Aug. 2020, doi: 10.1109/TITS.2020.3012724.

[26] N. T. J. Bailey, "An introduction to stochastic processes: With special reference to methods and application," *J. Roy. Statistical Soc. Ser. A (General)*, vol. 118, no. 4, pp. 484–485, Jul. 1955, doi: 10.2307/2342717.

[27] M. S. Sharawi, "Current misuses and future prospects for printed multiple-input, multiple-output antenna systems [Wireless Corner]," *IEEE Antennas Propag. Mag.*, vol. 59, no. 2, pp. 162–170, Apr. 2017, doi: 10.1109/MAP.2017.2658346.

[28] M. Ghaddar, M. Nedil, I. B. Mabrouk, and L. Talbi, "Multiple-input multiple-output beam-space for high-speed wireless communication in underground mine," *IET Microw., Antennas Propag.*, vol. 10, no. 1, pp. 8–15, Jan. 2016, doi: 10.1049/iet-map.2014.0464.

[29] G. J. Foschini and M. J. Gans, "On limits of wireless communications in a fading environment when using multiple antennas," *Wireless Personal Commun.*, vol. 6, no. 3, pp. 311–335, Mar. 1998, doi: 10.1023/A:1008889222784.

[30] Y. Jiang, G. Zheng, X. Yin, A. Saleem, and B. Ai, "Performance study of millimetre-wave MIMO channel in subway tunnel using directional antennas," *IET Microw., Antennas Propag.*, vol. 12, no. 5, pp. 833–839, Apr. 2018, doi: 10.1049/iet-map.2017.0338.

MEETINGS & SYMPOSIA

ANTENNA MEASUREMENT TECHNIQUES ASSOCIATION ANNUAL MEETING AND SYMPOSIUM (AMTA 2022)

9–14 October 2022, Denver, Colorado, United States. http://www.amta2022.org.

59th ANNUAL AOC INTERNATIONAL SYMPOSIUM AND CONVENTION

25–27 October 2022, Washington, District of Columbia, United States. Amy Belicev, Association of Old Crows, 1555 King Street, Suite 500, Alexandria, VA 22314, United States. +1 703 549 1600; email: belicev@crows.org. http://www.crows.org.

SECOND INTERNATIONAL CONFERENCE ON ELECTRICAL, COMPUTER, COMMUNICATIONS AND MECHATRONICS ENGINEERING (ICECCME)

16–18 November 2022, Male, Maldives. (Papers: 10 June 2022.) HYBRID CONFERENCE. http://www.iceccme.com.

IEEE GLOBAL COMMUNICATIONS CONFERENCE (IEEE GLOBECOM 2022)

4–8 December 2022, Rio de Janeiro, Brazil. (Papers: 15 April 2022). HYBRID CONFERENCE. Conference information: email: j.le@comsoc.org. http://globecom2022.ieee-globecom.org/.